Subduction of carbon, nitrogen, and oxygen in the northeast Atlantic

Pierre Karleskind, Marina Lévy, Laurent Mémery

Subduction of carbon, nitrogen, and oxygen in the northeast Atlantic

P. Karleskind,[1] M. Lévy,[2] and L. Memery[1]

Received 10 June 2010; revised 19 October 2010; accepted 17 November 2010; published 17 February 2011.

[1] Northeast Atlantic mode waters (NEAMW) are formed by subduction in a region known to be a strong sink of atmospheric CO_2. This study investigates the biological and physical carbon pumps involved in this sink. For that purpose, we estimate the annual transfer of carbon, nitrogen, and oxygen from the surface into the ocean interior through NEAMW subduction. Our estimates are based on a model simulation constrained with data collected during the Programme Océan Multidisciplinaire Méso Echelle (POMME). We found that subduction accounts for a large proportion of carbon export below the mixed layer in the POMME region (38°N–45°N, 16°W–22°W). Fifty percent of labile organic carbon is exported by the biological pump and 50% by subduction; 98% of the total carbon flux below the mixed layer is due to carbon subduction, essentially in the form of dissolved inorganic carbon and of more refractory dissolved organic matter. This is because they are the dominant pools of carbon and are passing through the winter mixed-layer depth gradient that characterizes the region. Our results emphasize that the net export of carbon represents a small fraction of the fluxes of carbon across the mixed layer through the processes of subduction and obduction. Moreover, our results indicate that NEAMW subduction occurs before the spring bloom. This implies that NEAMW is mostly subducted with end-winter characteristics with, in particular, relatively high nutrient content. This reflects a relative inefficiency in nutrient utilization and contrasts with subtropical mode waters, which are subducted during the bloom and are thus relatively poor in nutrients when they are subducted.

Citation: Karleskind, P., M. Lévy, and L. Memery (2011), Subduction of carbon, nitrogen, and oxygen in the northeast Atlantic, *J. Geophys. Res.*, *116*, C02025, doi:10.1029/2010JC006446.

1. Introduction

[2] Oceanic subduction is the process by which water masses escape the surface of the ocean and penetrate into the interior. Water masses are formed in the surface mixed layer and acquire their characteristics through the exchange of heat, moisture, and dissolved gases with the atmosphere. Once water masses are subducted, they are shielded from the influence of the atmosphere. Subduction is thus of primary importance for the oceanic carbon cycle. On one hand, it removes CO_2 from the ocean surface and exports it to the interior. On the other hand, it sets the biogeochemical characteristics of the subsurface nutrient reservoirs, with implications for ocean productivity [*Sarmiento et al.*, 2004].

[3] In the northeast Atlantic, the southern branch of the North Atlantic current (Figure 1) flows southward across a strong gradient of winter mixed-layer depth (MLD) near 42°N [*de Boyer Montegut et al.*, 2004]. These conditions induce the subduction of the 11°C–13°C mode waters at the end of winter [*Paillet and Arhan*, 1996], also known as northeast Atlantic mode waters (NEAMW) [*Reverdin et al.*, 2005]. These relatively dense waters are southwardly advected at the subsurface.

[4] This MLD gradient also divides the region into an oligotrophic zone in the south and a biologically productive area in the north [*Lévy et al.*, 2005a]. In the northern area, characterized by a deeper MLD and a well-marked bloom, primary production consumes inorganic carbon. This initializes the biological pump of CO_2. Subduction and the spring bloom occur approximately at the same period, between winter and spring. The precise knowledge of the mechanisms driving subduction and of the timing of subduction versus the timing of the spring bloom are crucial to assess the transfer of carbon from the atmosphere to the ocean interior.

[5] The area of NEAMW formation is known to act as a sink of atmospheric CO_2 [*Takahashi et al.*, 1995; *Rios et al.*, 1995]. This study aims to investigate the different processes involved in this CO_2 sink, in particular the biological and physical carbon pumps and their coupling. Specifically, we address the following questions: (1) How and when does subduction operate in this region and does it remove carbon, nitrogen, and oxygen from the mixed layer? (2) What is the

[1]LEMAR, CNRS/IRD/UBO, Brest, France.
[2]LOCEAN/IPSL, CNRS/UPMC/IRD/MNHN, Paris, France.

0148-0227/11/2010JC006446

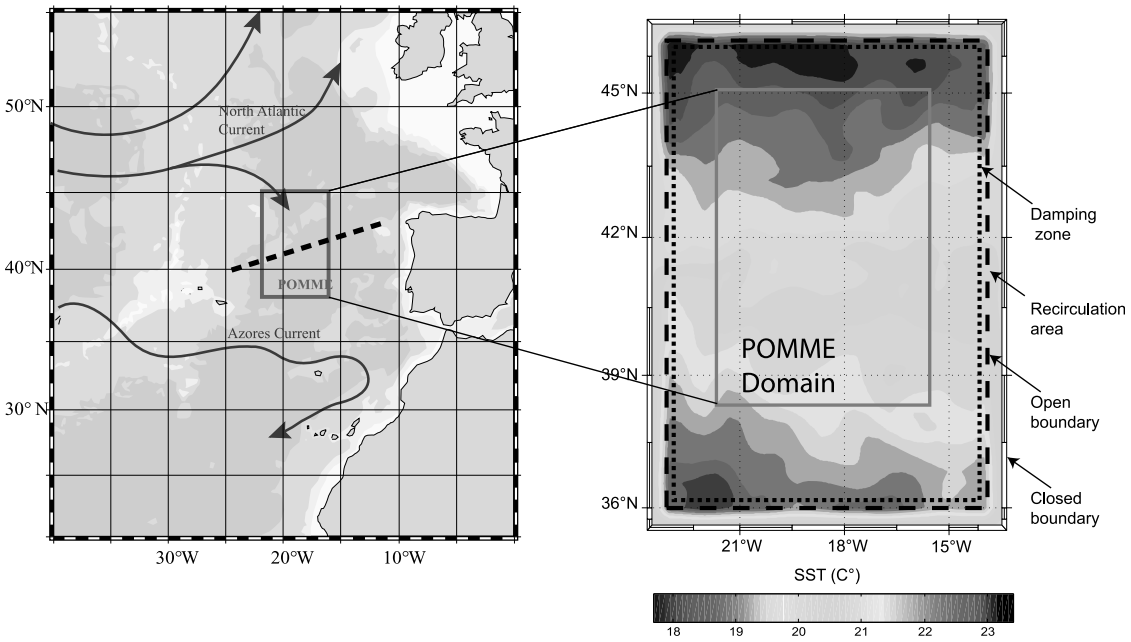

Figure 1. Location of the POMME domain. (left) Topography (shading) with a schematic representation of the main currents (arrows) and of the strongest gradient in winter mixed-layer depth (dashed line); (right) initial sea surface temperature field in the model (27 September 2000), issued from the Mercator MERA-11 reanalysis. The damping zone of the model is shown between the dotted line and the open boundary (dashed line). The recirculation area is between the open boundary and a closed boundary.

efficiency of the physical carbon pump compared to that of the biological carbon pump? (3) What are the biogeochemical characteristics of NEAMW and to what extent do they fuel the subtropical gyre's thermocline with nutrients?

[6] This study is based on the Programme Océan Multidisciplinaire Méso Echelle (POMME) experiment [*Memery et al.*, 2005], during which four oceanic cruises were conducted over one annual cycle in the northeast Atlantic. A 1 year high-resolution bio-physical simulation of the region covered by the POMME experiment is performed, with precise diagnostics of kinematic subduction rates of water, carbon, nitrogen, and oxygen. In section 2, the POMME experiment and model configuration are presented. In section 3, the model simulation is evaluated with data collected during POMME cruises. The subducted water masses are then characterized in section 4. Finally, the computed values for subduction and for the various fluxes are discussed in section 5.

2. Context and Method

2.1. The POMME Experiment

[7] The POMME experiment aimed to investigate the subduction and biogeochemical properties of NEAMW [*Memery et al.*, 2005]. From fall 2000 to fall 2001, four oceanographic cruises (P0, 20 September to 13 October; P1, 3–23 February; P2, 24 March to 12 April; P3, 23 August to 14 September) covered a rectangular 750 km × 500 km region of the eastern North Atlantic between 38°N and 45°N (Figure 1). Each cruise was divided into two legs. During the first legs, conductivity-temperature-depth and expendable bathythermograph casts were performed with a resolution of 55 km between stations and samples were collected in the upper 400 m. These samples were used to measure the concentrations of the main tracers (nutrients, O_2, pigments, and bacterial biomass) as well as phytoplankton diversity, primary production, and grazing. The full area was covered in approximately 3 weeks during the first legs. The second legs were designed for small-scale surveys and for 1-D biogeochemical process studies [nutrients, O_2, dissolved inorganic carbon (DIC), dissolved organic carbon (DOC), primary production, and carbon and oxygen balances]. Net tows were used to sample zooplankton in the upper 200 m and sediment traps were deployed during 2 day quasi-Lagrangian time-series stations. (POMME data are available at http://www.obs-vlfr.fr/proof.)

2.2. Model Configuration

[8] The model configuration is adapted from that of *Lévy et al.* [2005b] and *Resplandy et al.* [2009], which focused on the 3 month evolution of the spring bloom over the POMME area. Here the simulations were extended to cover the full year from fall 2000 to fall 2001. The domain of computation extends from 36°N to 46°N and from 14°W to 23°W, which corresponds to the surveyed area with approximately 2° added on each side (Figure 1). The vertical resolution is 5 m in the upper 150 m and there are 69 vertical levels. The horizontal resolution (1/25° in the N–S direction and 1/20° in the E–W direction) enables the representation of the numerous mesoscale eddies present in the area and of their interactions. The choice of an eddy-resolving simulation is dictated by the results of *Paci et al.* [2007], which showed that small physical transport contributed significantly to the subduction budget during POMME. The details of the mesoscale and submesoscale are not examined in this paper and can be

found in the work by *Karleskind et al.* [2011]. Here the focus is on the large-scale budgets.

[9] Surface forcings are derived from combined satellite and in situ meteorological data, weather model outputs, and specific bulk formulas deduced from measured turbulence [*Caniaux et al.*, 2005]. A sponge layer surrounds the interior domain of computation (Figure 1). In this layer, temperature, salinity, and biogeochemical tracers are restored toward prescribed values. Open boundaries are ensured by embedding the whole configuration within a recirculation area following the methodology of *Gavart et al.* [1999].

[10] The NEMO primitive equation ocean model is used, in its rigid-lid version (OPA 8.2). Vertical turbulence is parameterized with a 1.5 turbulent closure model based on a prognostic equation of turbulent kinetic energy [*Gaspar et al.*, 1990]. A bi-Laplacian operator is used for temperature, salinity, and momentum diffusion, with a dissipation coefficient $|K_h| = 1.5 \times 10^9$ m^4 s^{-1}. The time step is 200 s and outputs are daily averages. The simulation begins on 27 September 2001 and lasts 384 days.

[11] The LOBSTER biogeochemical model is embedded within the physical model. LOBSTER solves the evolution of nine biogeochemical variables: phytoplankton, zooplankton, detritus, semilabile dissolved organic material (DOM), nitrates, ammonium, DIC, alkalinity, and oxygen. It is described in the appendix.

2.3. Initial and Boundary Conditions

[12] Initial and boundary conditions for temperature (T) and salinity (S) are taken from the Mercator MERA-11 reanalysis of the North Atlantic. This reanalysis was performed by the operational oceanography center Mercator-ocean with the same primitive equation model, on a 1/3° grid. It includes sequential assimilation of altimetry and of in situ observations of T and S profiles (including those acquired during POMME). The weekly outputs of T and S provided by MERA-11 were then interpolated in time at each model time step at the model open boundaries.

[13] For biogeochemical tracers, no equivalent reanalysis is available and spatiotemporal extrapolation of POMME observations was used. We followed the same methodology as *Lévy et al.* [2005b]. Nitrates, DIC, alkalinity, and oxygen data acquired during the first legs of each POMME cruise were first interpolated onto the model grid inside the domain of survey. Then they were extrapolated outside this domain. This was done in the following way: at each latitude, the zonal mean of all fields inside the domain of survey was applied on the east and west sides of the domain. This choice was motivated by the observed distribution of the fields inside the survey area, which exhibited a variability dominated by strong meridional gradients. For the same reason, at the northern and southern boundaries, values were extrapolated by prolonging the mean meridional gradient. The extrapolation of P0 data provided the initial fields. For DOM, we had no direct observations and estimated the initial semilabile fraction of DOM as a constant fraction (40%) of total organic carbon, which was measured during POMME [*Sohrin and Sempéré*, 2005]. Given their rapid response time, phytoplankton, ammonium, detritus, and zooplankton were uniformly initialized to 0.1 mmolN m^{-3}. At the boundaries, they were simply damped toward instantaneous zonal means (in the case of western and eastern boundaries) or zonal mean of the last or first line inside the domain (in the case of the northern or southern boundaries, respectively). This was also the case for DOM.

[14] To provide boundary conditions for DIC, nitrates, and alkalinity, extrapolated cruise data were linearly interpolated in time between P0 and P1, P1 and P2, and P3 and P0. However, linear interpolation is not suitable between P2 and P3, which are 5 months apart, given that the spring bloom occurred mostly during P2: it cannot account for the rapid utilization of nutrients associated with the bloom and tends to strongly overestimate the postbloom nutrient concentrations. Thus, to account for the rapid nutrient drawdown associated with the bloom in the boundary conditions, after 4 April 2001 (median date of P2, during which the bloom occurs), nitrates, alkalinity, DIC, and oxygen were damped toward T_d, a linear combination of the zonal means and of the P3 values [$T_d = \frac{t-t_{P3}}{t_{P2}-t_{P3}} T_{\text{zonmean}} + (1 - \frac{t-t_{P3}}{t_{P2}-t_{P3}})\, T_{P3}$, where t is the current time, t_{P2} and t_{P3} are the median dates of P2 and P3, T_{zonmean} is the zonal mean of tracer T at time t, and T_{P3} is the value T at time t_{P3}].

2.4. Subduction Diagnostics

[15] Three physical processes may lead a water parcel to leave the surface mixed layer: vertical advection, horizontal advection, and mixed-layer detrainment. More precisely, following the work of *Cushman-Roisin et al.* [1987], the total instantaneous subduction rate can be defined as $s(t) = s_w(t) + s_{\text{ind}}(t) + s_h(t)$, where $s_w(t) = -w_h$ is the contribution of vertical advection, $s_{\text{ind}}(t) = -\vec{u}_h \cdot \vec{\nabla} h$ is the contribution of horizontal advection (also referred to as lateral induction), and $s_h(t) = -\frac{\partial h}{\partial t}$ is the contribution of the mixed layer trend (also referred to as detrainment when positive and as entrainment when negative), with h the mixed-layer depth and $\vec{u}_h$ and w_h the horizontal and vertical velocities, respectively, at the base of the mixed layer. By convention, subduction corresponds to positive values of s (water exiting the mixed layer) and obduction to negative values of s (water entering the mixed layer). At time T, the cumulated subducted water (per surface unit) is $S(T) = \int_0^T s(t)dt$. The annual subduction rate is $S_{\text{ann}} = \int_0^{365} (-w_h - \vec{u}_h \cdot \vec{\nabla} h - \frac{\partial h}{\partial t})dt$. In the annual integration, the third term of the integral is equal to the MLD interannual trend.

[16] The instantaneous subduction rate for the different tracers can be defined similarly, as the flux of tracer crossing the mixed layer. Let c_h be the concentration of a tracer TR at the mixed-layer base. The instantaneous flux of tracer across the mixed layer per surface unit via advection is $c_h(t) \cdot s(t)$. In addition, one must also consider the effect of vertical diffusion. Indeed, diffusive processes, which do not lead to a net volume flux, may lead to a nonzero flux of tracers across the mixed-layer base. Lateral diffusion was very small in our high-resolution experiment and we neglected it. In consequence, the amount (per surface unit) of tracers that annually subduct is given by

$$S_{\text{ann}}^{\text{TR}} = \int_0^{365} \left(-c_h \cdot w_h - c_h \cdot \vec{u}_h \vec{\nabla} h - c_h \cdot \frac{\partial h}{\partial t} - A_z^h \cdot \frac{\partial c_h}{\partial z} \right) dt,$$

with A_z^h the vertical eddy diffusivity coefficient. The computation of these different terms was implemented online for each tracer in the model. The criterion used to define the bottom of the mixed layer is a density difference with the surface larger than 0.01. Moreover, as subduction is an

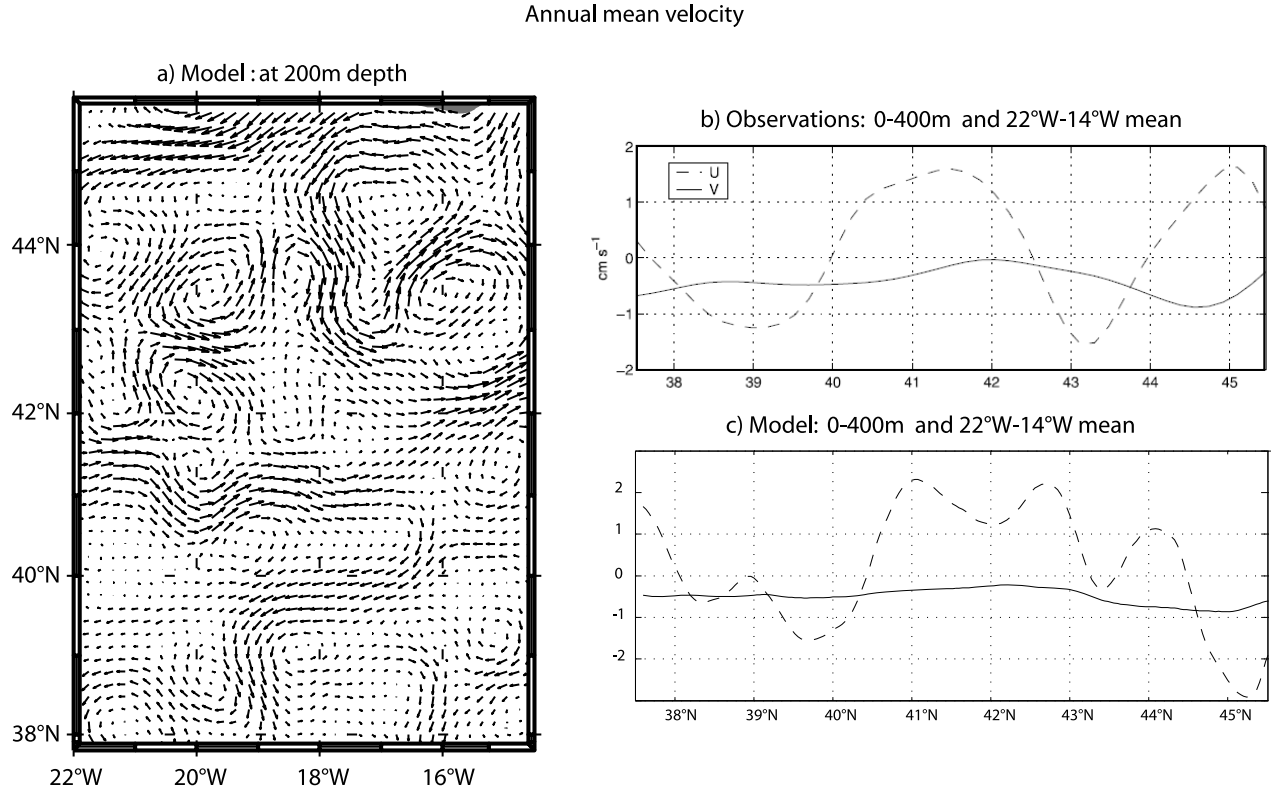

Figure 2. (a) Annual mean velocity in the model at 200 m depth. (b and c) Latitudinal variations of the annual mean velocity averaged over 0–400 m and along the zonal direction: Figure 2b shows observations (reanalysis of in situ measurements by *Gaillard et al.* [2005] and partial reproduction of their Figure 11), and Figure 2c is in the model.

isopycnic process, it is relevant to compute the subduction rates following the instantaneous potential density ranges in the mixed layer. Thus in addition, subduction of water, nitrates, oxygen, and DIC were computed in the density classes between 1026.35 and 1027.15, with an increment of 0.05.

3. Model Evaluation

[17] Here we focus on the physical and biogeochemical fields which are directly involved in the subduction budgets, i.e., the circulation of the upper 400 m, the mixed-layer depth, and the evolution of phytoplankton, inorganic nutrients, and oxygen. Our simulation is fully prognostic, with no data assimilation. This implies that, because the simulation lasts 1 year, the precise location of the mesoscale structures in the model is not guaranteed. Thus, the model results cannot be synoptically compared with POMME observations. For that reason, the evaluation is presented over statistical properties of the fields (meridional averages and standard deviation).

3.1. Physics

[18] The model annual mean circulation in the upper 400 m is characterized by a zonal jet which crosses eastwardly the area between 41°N and 42°N with mean values reaching 5 cm s^{-1} (Figure 2a and dashed line in Figure 2c). This jet retroflects southward between 16°W and 18°W, and five or six persistent eddies fill the northern part of the domain. There is a mean southward circulation, which varies between 0.2 and 0.9 cm s^{-1} (Figure 2c, solid line). This mean circulation pattern is consistent with that derived from POMME observations [*Gaillard et al.*, 2005] (Figure 2b). There is one exception, however, north of 44°N, where the simulated circulation is westward while it is eastward in the observations. The model mean eddy kinetic energy is around 38 cm^2 s^{-2}, close to the estimate of *Gaillard et al.* [2005] (40 cm^2 s^{-2}).

[19] The simulated mixed layer (Figure 3a) displays a marked seasonal cycle, with a deepening from September to February, followed by restratification in March and April. Restratification is interrupted by a storm in mid-April before complete restratification in summer. The area is characterized by a strong meridional gradient in wintertime MLDs, with maximum MLD in the north of the domain deeper than in the south (150 m versus 80 m on average). This seasonality and latitudinal gradient are in fair agreement with in situ estimates of the mixed layer (Figure 3a), given the large MLD variance and asynopticity of the data [*Memery et al.*, 2005; *Paci et al.*, 2005; *Lévy et al.*, 2005b].

3.2. Biogeochemistry

[20] The POMME area is the scene of a medium-amplitude phytoplankton bloom, with chlorophyll concentrations reaching 1–2 mgChl m^3 in spring (Figure 4). The bloom starts in the south of the domain in late winter and progresses toward the north during spring in response to the stratification of the

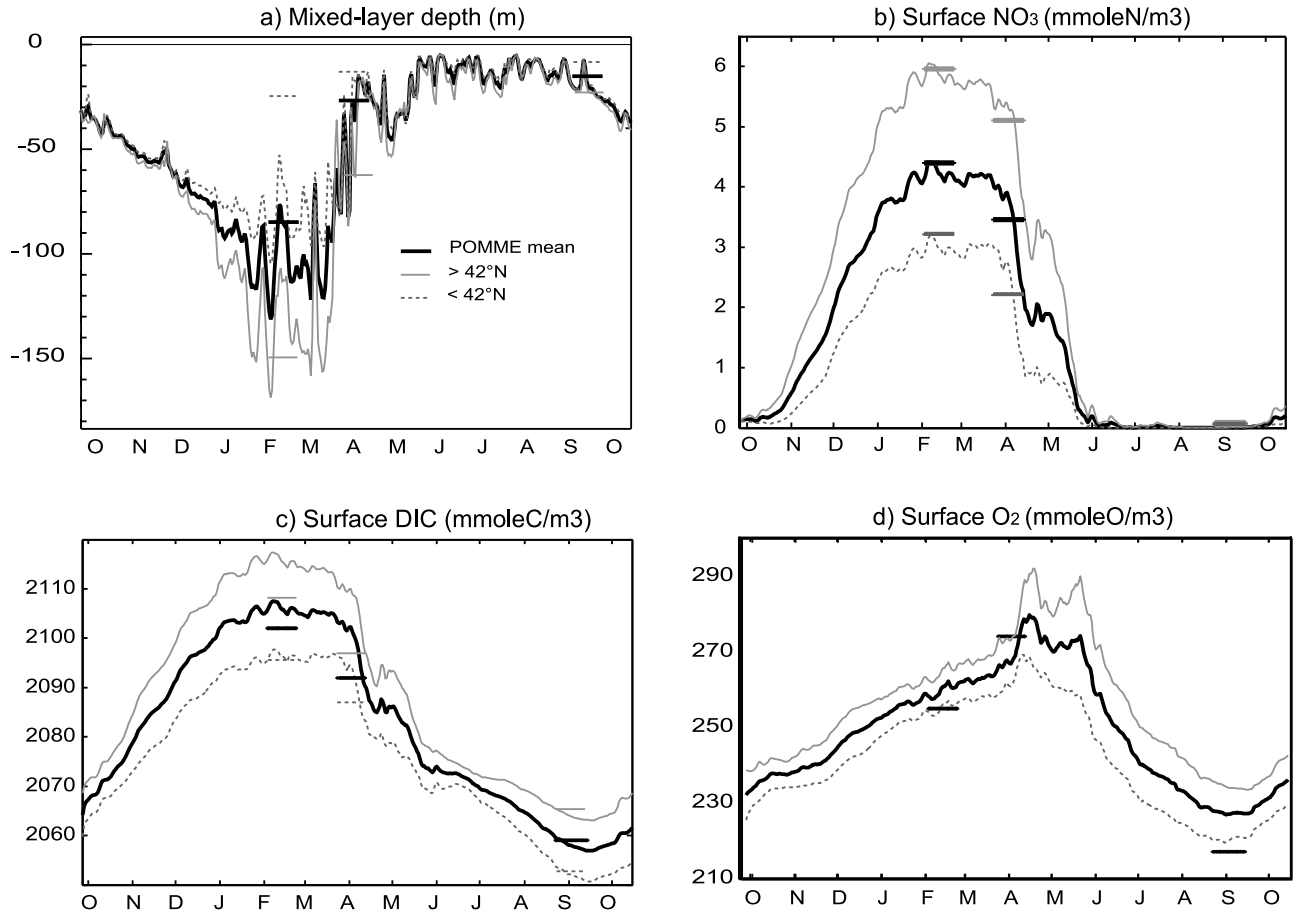

Figure 3. Time evolution of (a) mixed-layer depth, (b) nitrate, (c) dissolved inorganic carbon (DIC), and (d) oxygen at the surface in the model and in POMME data. The thick line shows the average concentration over the POMME domain, and the shaded and dotted lines show the average concentration in the north and south of the domain, respectively. POMME measurements during the first legs of P1, P2, and P3 are shown as horizontal lines. The length of the line indicates the duration of the leg.

mixed layer. In 2001, the bloom was briefly interrupted during a storm in April. The comparison of the model zonal mean surface chlorophyll concentration with Sea-viewing Wide Field-of-view Sensor (SeaWiFS) observations shows that the bloom evolution and amplitude are well simulated (Figure 4). We note, however, that the amplitude of the second stage of the bloom in May (i.e., after the storm) is weaker than observed, probably due to the underestimation of the vertical entrainment of nutrients driven by the storm [*Lévy et al.*, 2005b]. This shortcoming should not strongly affect subduction rate estimates since subduction involves water masses present at the surface before late winter restratification rather than being dependent on conditions later in the season.

[21] The evolution of nitrates and DIC in the mixed layer (Figures 3b and 3c) shows an increase until February, associated with the deepening of the mixed layer, followed by a decrease due to their consumption by phytoplankton during the bloom. The concentrations are higher in the north than in the south, mainly because of the deeper mixed layers in winter. Comparison with observations during the first legs of the POMME cruises shows that the amplitude and timing of the seasonal variations of surface nitrate and DIC are well captured by the model (Figures 3b and 3c). POMME observations also provide estimates of the mean vertical profiles of DIC and nitrates at three different periods of the year (solid lines in Figure 5: P1L1, P2L1, and P3L1). In winter, during P1L1, the profiles are homogeneous within the mixed layer (down to 100 m on average). During P2L1, the mean profiles show that consumption has started at the surface (below 50 m on average). The profiles during P3L1 show a strong vertical gradient (between 50 and 100 m) between surface depleted waters and rich subsurface waters. The model mean profiles agree with these general characteristics. We note a slight overestimation of nitrates and DIC between 50 and 100 m in summer in the model. Again, this should not affect our subduction diagnosis since it is after subduction has occurred. During P2L1, the model profiles at the beginning and end of the leg differ, owing to the spring bloom occurring during P2L1: this highlights the strong asynopticity of the P2L1 data set, already noted by *Memery et al.* [2005]. As expected, the O_2 profiles are anticorrelated with the NO_3 and DIC profiles. During summer, because of the relatively high air-sea gas exchange, and because of the sea surface temperature increase, dissolved O_2 tends to escape the mixed layer toward the atmosphere, which explains its decrease above 60 m and the relative maximum at 60 m.

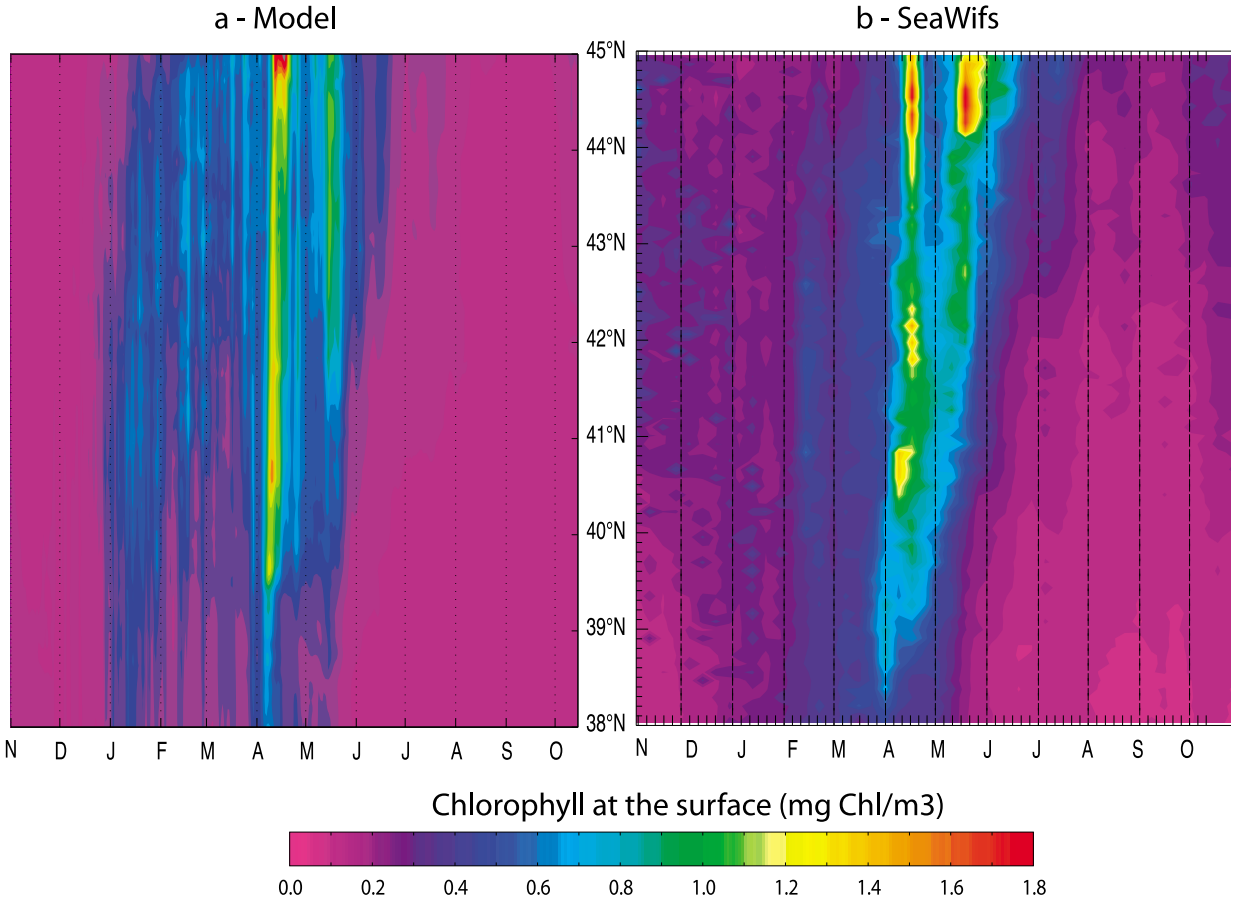

Figure 4. Evolution of the zonal mean chlorophyll at the sea surface between November 2000 and November 2001 (a) simulated by the model and (b) observed by the Sea-viewing Wide Field-of-view Sensor (SeaWiFS).

[22] The net, daily mean, 0–100 m primary production (PP) progressively increases from December to April (Figure 6c) and reaches a maximum of 10 mmolN m^{-2} d^{-1}. Comparison with in situ measurements shows that the simulated PP is in the upper range of the measurements during P1L1 and P2L1 and is too low during P3L1. The *f* ratio (not shown) is also in good agreement with the observations: from mid-January until May, it increases from 0.45 to 0.7, and it decreases again below 0.4 in summer. When compared to measurements by drifting sediment traps at 200 m depth, the export by sedimentation in the model is higher by approximately a factor of 2 (not shown). This could be due to the underestimation of the measured export during POMME as noted by *Goutx et al.* [2005] and *Guieu et al.* [2005] or to the lack of export through a longer-lived form of DOM in our model. Regarding semilabile DOM, we lacked observations to evaluate the behavior of the model. However, after 1 year, the model adjusted to a value approximately two thirds lower than the initial condition that we used, suggesting that our first guess for DOM initialization was overestimated. This extra DOM in our initial state could explain the overestimation of nitrates and DIC between 50 and 100 m that we obtain in summer. In conclusion, the physical simulation is satisfying in terms of mean circulation and mixed-layer dynamics. This allows us to compute subduction rates with good confidence. Despite some unsatisfying behavior of the biological model during late summer and some uncertainties regarding DOM and export, our simulation is in good agreement with the POMME winter and spring observations. It can thus be reliably used to compute the tracer subduction budgets of the POMME area.

4. Results

4.1. Water Subduction

[23] The net subduction after 1 year computed from the model is 33.6 m yr^{-1} (33.6 m^3 m^{-2} yr^{-1}) for the POMME area (Table 1). Over the POMME domain (3.6×10^{11} m^2), this represents a net transport of 0.38 Sv toward the ocean interior. This estimate falls in the range of previous estimates for the same region [*Marshall et al.*, 1993; *Giordani et al.*, 2005; *Gaillard et al.*, 2005, *Valdivieso da Costa et al.*, 2005].

[24] On an annual average, the contribution of the mixed-layer trend to the net subduction is small (−1.1 m, Table 1) because the mixed layer nearly comes back to its initial depth after 1 year (Figure 3a). In fact, the 33.6 m of subducted waters result essentially from the balance between lateral induction (59 m, Table 1) and vertical advection (−24 m, Table 1). In our simulation, the vertical velocity is the sum of a large-scale component, due to Ekman pumping and ori-

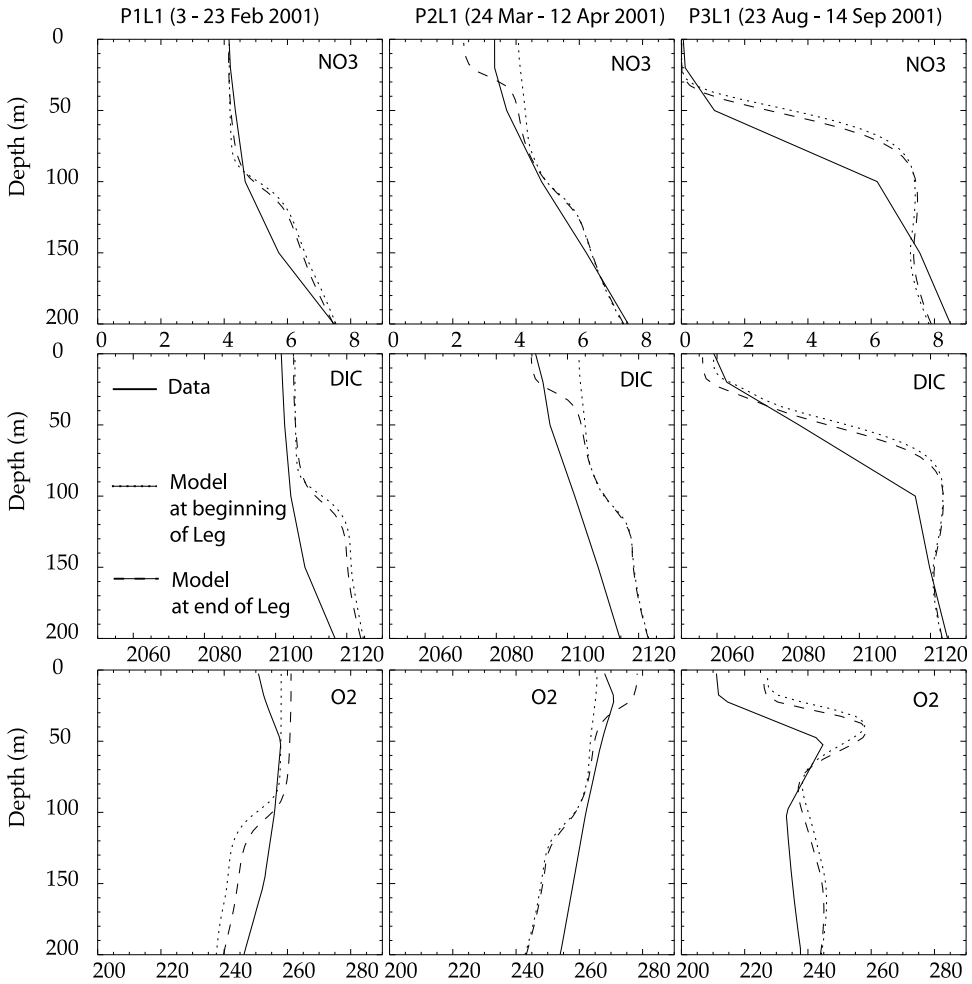

Figure 5. Vertical profiles of nitrate, DIC, and oxygen during the first legs of P1, P2, and P3. The solid line shows the mean profile in the observations, and the dotted and dashed lines show the mean profile in the model at the beginning and at the end of the leg, respectively. Units are mmolN/m^3, mmolC/m^3, and mmol O/m^3.

ented downward, and of up-and-down motions within submesoscale filaments, much larger in amplitude than Ekman pumping [*Paci et al.*, 2007]. The contribution of vertical advection in our simulation reflects the predominant role of submesoscale vertical velocities since it has the opposite sign than what would be expected from Ekman pumping alone [*Karleskind et al.*, 2011].

[25] The time evolution of the cumulated subducted water reveals a strong seasonality in the process of subduction (Figure 6a). This seasonality is driven by the seasonality of the mixed layer. From October to February, there is obduction of 100 m of water caused by the deepening of the mixed layer. During that period, the north–south mixed-layer gradient establishes itself (Figure 3a) and lateral induction comes into play, causing a positive contribution to subduction. Between February and early April, the period of effective detrainment takes place. The shallowing of the mixed layer leads to the subduction of about 100 m of water. During this period, the north–south mixed-layer gradient is still there but progressively vanishes (Figure 3a and dashed line in Figure 8a); lateral induction and vertical advection remain active. After that, from mid-April to September, the cumulated subducted water follows the small variations of the mixed layer, and the contributions of lateral induction and vertical advection are small. There is, in particular, an event of obduction followed by subduction associated with a storm in late April.

4.2. Subduction of NEAMW

[26] Waters that obduct and waters that subduct have different density characteristics. This is shown in Figure 7a, which shows the net subduction/obduction against density. The general pattern is that low-density waters ($\sigma < 26.4$) are obducted, essentially from October to February, through mixed-layer entrainment (Figure 6a); these light water masses are transformed at the surface into denser waters in response to forcing by the atmosphere; on the other hand, waters that subduct, essentially from February to early April (Figure 6a), are mainly in the high-density range ($\sigma > 26.85$). We can also note that waters in the density range 26.75–26.85 have a specific subduction scheme. They have relatively high densities but tend to obduct like light waters. These waters are, in fact, involved in the storm that occurred in late April.

[27] The highest subduction rates are found for the water masses whose densities are in the range between 26.85 and

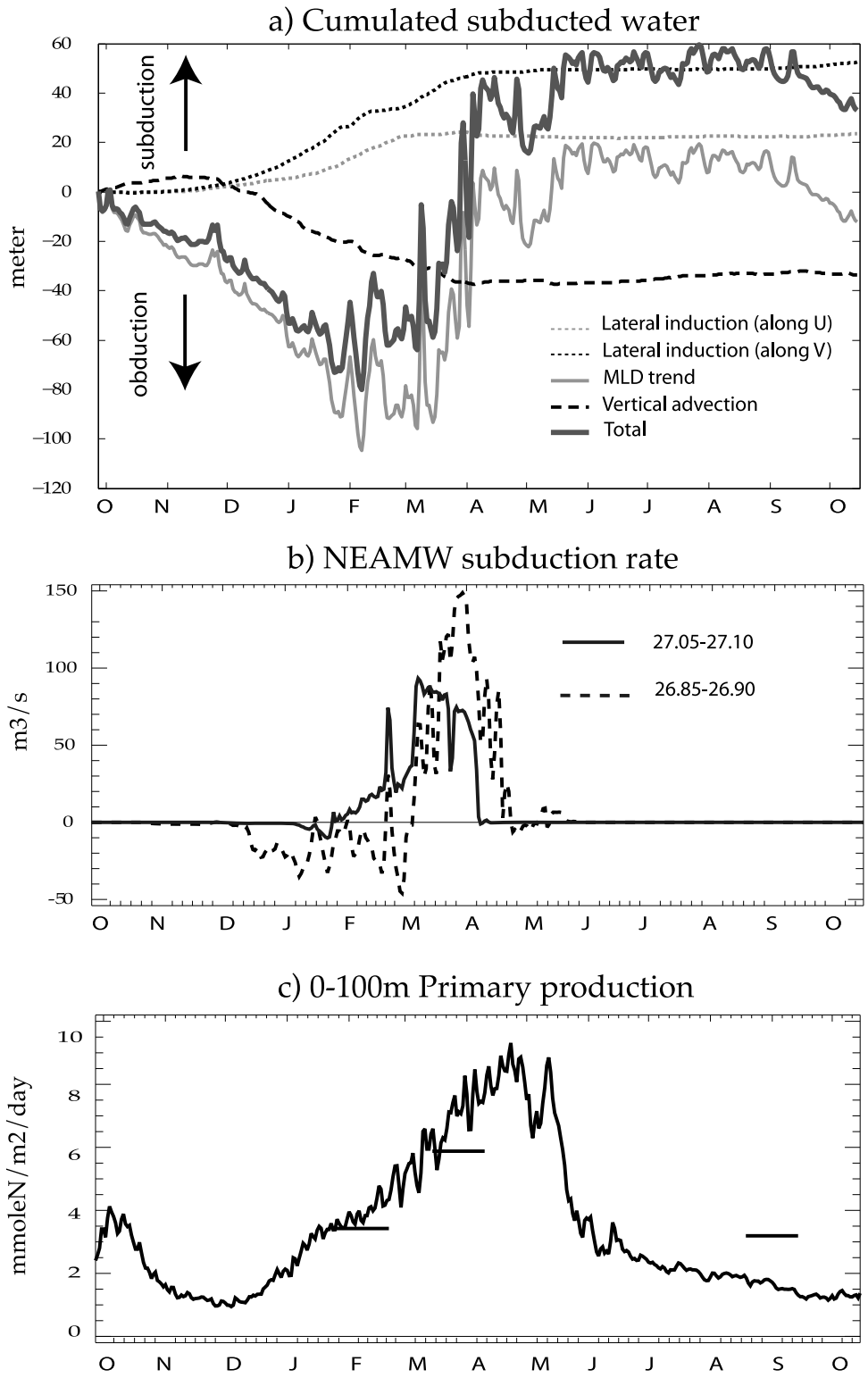

Figure 6. (a) Time evolution of the total cumulated subducted water. The different curves show the contributions of the different processes involved. (b) Subduction rate of NEAMW in the 27.05–27.10 and 26.85–26.90 density ranges. The subduction rates were averaged over the POMME domain and then smoothed in time with a boxcar average of 1 month width. (c) Net primary production (the horizontal lines show the mean primary production measured during P1L1, P2L1, and P3L1).

Table 1. Subduction Budgets Over 1 Year[a]

		Inorganic Tracers			Organic Tracers	
	Water (m)	O_2 (mol O m^{-2})	DIC (mol C m^{-2})	DIN (mmolN m^{-2})	OC (mol C m^{-2})	ON (mmolN m^{-2})
Diffusion		0.95	−2.1	−307.7	0.66	96.2
MLD	−1.1	2.0	−1.0	155.3	0.34	47.8
Vert. advection	−24	−6.6	−60	−262.8	0.16	21.8
Lat. induction	59	16.1	126.7	253.0	0.36	44.2
Total	33.6	12.3	64	−162	1.5	210

[a]DIC, dissolved inorganic carbon; DIN, dissolved inorganic nitrogen (nitrate + ammonium); MLD, mixed-layer depth; OC and ON, organic carbon and organic nitrogen (phytoplankton + zooplankton + detritus + semilabile dissolved organic matter). For organic tracers, a C:N ratio of 6.625 mol C mol N^{-1} is used for phytoplankton, zooplankton, and detritus; a ratio of 12 mol C mol N^{-1} is used for semilabile DOM.

27.10. In winter, these waters were found in the surface mixed layer north of 42°N (Figure 8a). In spring, they were below the mixed layer, extended as far south as 40°N and were characterized by their low potential vorticity (PV) (Figure 8b). These characteristics (subsurface waters with density around 27 and low PV) are those of the NEAMW [*Reverdin et al.*, 2005]. Our model results thus confirm that subduction within the POMME domain contributed to the formation of NEAMW. Figure 8 illustrates that NEAMW were formed north of 42°N between winter and spring and were then slowly advected to the south by the mean circulation.

[28] It is during the subduction period that water masses acquire their characteristics. The main subduction period is usually defined as the period of effective detrainment [*Qiu and Huang*, 1995]. This is confirmed in our simulation and corresponds to the period extending from February to mid-April, during which the mixed layer retreats (Figure 3a) and the total cumulated subducted water increases (Figure 6a). However, a closer examination at the subduction rates of NEAMW reveals that the subduction period depends on the density of the water mass being subducted (Figure 6b). The densest NEAMW (27.05–27.10) subduct first, from February to the end of March (solid line in Figure 6b). The lightest NEAMW (26.85–26.90) subduct later, from March to mid-April (dashed line in Figure 6b).

4.3. Subduction of Inorganic Nutrients and of Labile Organic Matter

[29] Subduction of water is accompanied by the subduction of inorganic nutrients. Figure 7 shows how the subduction

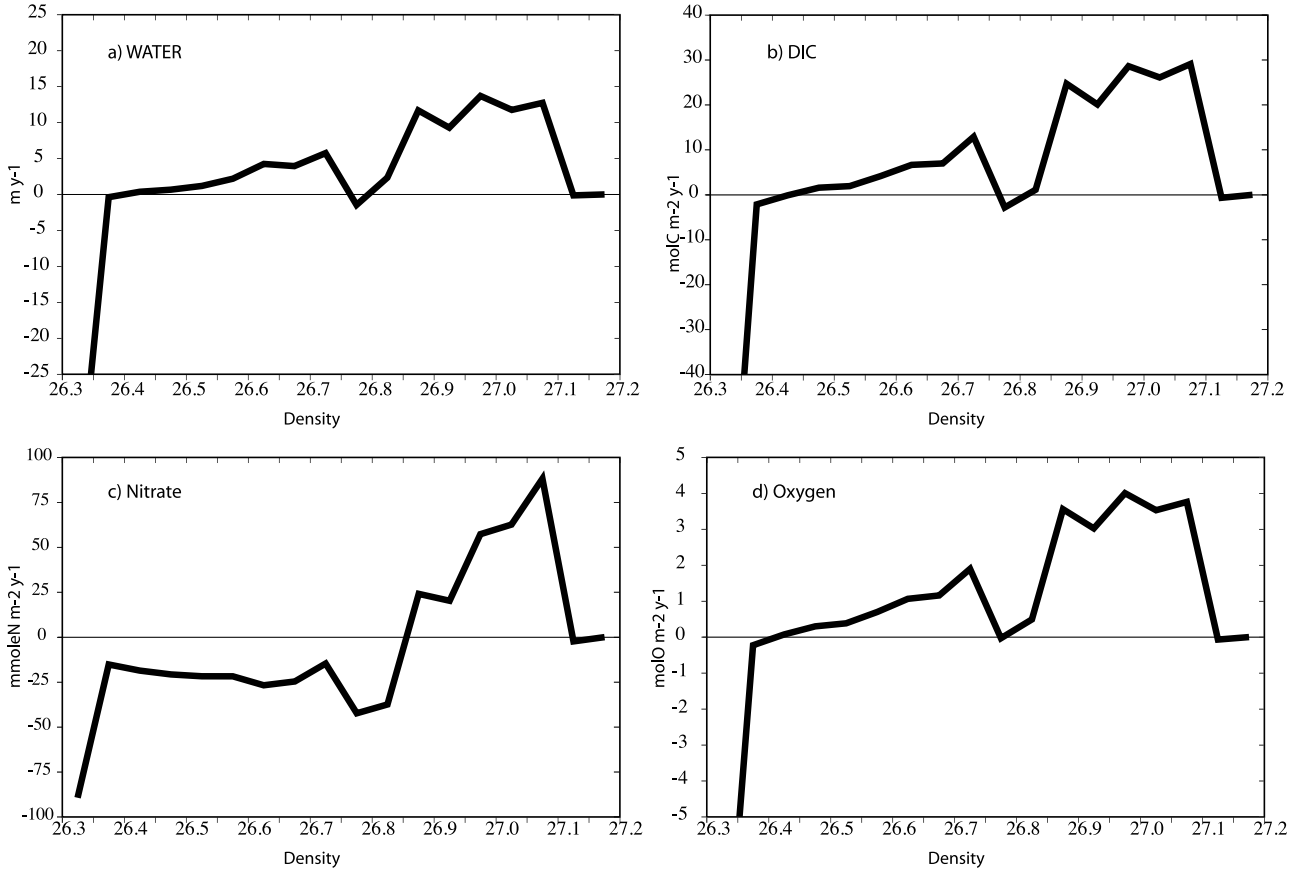

Figure 7. Total subducted (a) water, (b) DIC, (c) nitrate, and (d) oxygen for different density classes. The different lines show the contributions of the different processes. The first class includes density < 26.35. The increment between classes is 0.05.

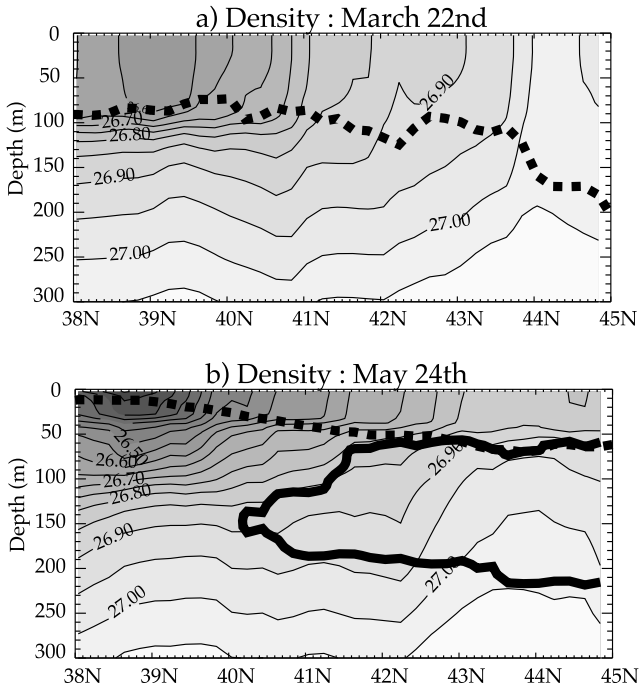

Figure 8. Vertical section of meridional mean density (a) during subduction (22 March) and (b) after subduction (24 May). The dashed line is the meridional mean mixed-layer depth. The thick contour delimits the area where potential vorticity is less than 1×10^{-12} m^{-1} and marks the location of NEAMW.

and obduction of inorganic nutrients are partitioned among the different density classes. The highest subduction rates for DIC, oxygen, and nitrates are reached in the density class of the mode waters (26.85–27.10).

[30] The general patterns in Figure 7 are similar for water, DIC, and oxygen: subduction in intermediate and dense waters (except in the density range 26.75–26.8) and obduction in light waters. Over 1 year, and averaged over all density classes, there is a net subduction of DIC (64 mol C m^{-2}, Table 1) and of oxygen (9.4 mol O m^{-2}, Table 1). The net subduction of DIC is the direct consequence of the net subduction of water. This is because DIC has low relative temporal variations over the year (±2%) and has a relative homogeneous distribution. We also note that the relative contributions of the various processes are in similar proportions for DIC and water, in particular with a predominant contribution of lateral induction (Table 1). The same holds for oxygen, whose distribution, like DIC, shows weak spatial and temporal relative variations. We can also note that, for DIC and oxygen, the diffusion term represents a weak contribution to the total subduction budget (Table 1).

[31] The situation is different for nitrates (Figure 7c), which are also subducted in dense waters and obducted in light waters, but which, unlike DIC and oxygen, are obducted in intermediate waters. In consequence, although nitrates subduct in NEAMW, there is a net obduction of nitrates over 1 year when averaged over all density classes (−82.8 mmolN m^{-2}). A similar result is found for ammonium, which represents the second form of inorganic nitrogen in the model (−79.1 mmolN m^{-2}). This leads to a net obduction of −162 mmolN m^{-2} of total dissolved inorganic nitrogen (DIN) in the model (Table 1). The obduction of nitrate in intermediate waters is due to the vertical diffusion term, which adds a positive contribution to obduction and reverses the total budget (not shown). The stronger contribution of the vertical diffusion of nitrate (Table 1) is linked to the fact that, except in winter, nitrates are rapidly consumed in the mixed layer, which creates a strong vertical gradient (Figure 5).

[32] Labile organic material (i.e., the sum of phytoplankton, zooplankton, detritus, and semilabile DOM in the model) is also exported below the mixed layer by subduction (Table 1). Over 1 year, 1.5 mol C m^{-2} are subducted under organic form, two thirds by diffusive processes and one third by advective processes. Subduction is shared between the different compartments, with a predominance of phytoplankton (50%) followed by zooplankton (20%) and semilabile DOM (20%). Note that this estimation is for labile organic matter and does not include subduction of more refractory forms of DOM. The contribution of refractory DOM, which is not explicitly accounted for in the model, is estimated in section 5.

[33] In total (organic and inorganic), there is a net subduction of carbon, nitrogen, and oxygen to the inner ocean in the model: 65.5 mol C m^{-2} yr^{-1} for carbon, 12.3 mol O m^{-2} yr^{-1} for oxygen, and 48 mmolN m^{-2} yr^{-1} for nitrogen (Table 1). The case for nitrogen is different because inorganic nitrogen is rapidly exhausted in the mixed layer. Nitrogen obducts in its inorganic form (nitrate and ammonium) and subducts in its organic form (phytoplankton, zooplankton, detritus, and DOM).

4.4. Biogeochemical Characterization of NEAMW

[34] The biogeochemical characteristics of NEAMW are depicted in Figure 9, which shows the scatterplot of DIC, nitrates, oxygen, and organic matter against density in the depth range of NEAMW after subduction. Dots corresponding to NEAMW (i.e., with low PV) are shown in black. At this time of the year, NEAMW are below the mixed layer (Figure 8b). In comparison with surrounding waters in the same depth range, NEAMW are characterized by the highest subsurface concentrations of oxygen and organic matter and the lowest concentrations of nitrate and DIC. This reflects the fact that NEAMW are young waters, which have been recently in contact with the atmosphere and in which remineralization has not yet taken place.

[35] The concentrations of nitrate and DIC within subsurface NEAMW cover a wide range: 4–8 mmolN m^{-3} for nitrate and 2105–2120 mmol m^{-3} for DIC (Figure 9). These biogeochemical characteristics of NEAMW ensue from the timing of the spring bloom versus the timing of subduction. Comparison of Figures 6b and 6c shows that the densest NEAMW (27.05–27.10) subduct mostly in March, i.e., 1 month before the peak of the bloom which occurs in April. Thus, this water mass is formed with prebloom, end-winter characteristics in terms of nitrate and DIC. This is confirmed in Figure 10, which shows the time evolution of nitrate and DIC in 27.05–27.10 waters when they are present at the surface. The concentrations remain approximately constant in time and there is no evidence of consumption by the bloom.

[36] The situation is slightly different for the lightest (26.85–26.90) NEAMW. They subduct mostly toward the end of March (i.e., only a couple of weeks before the peak of

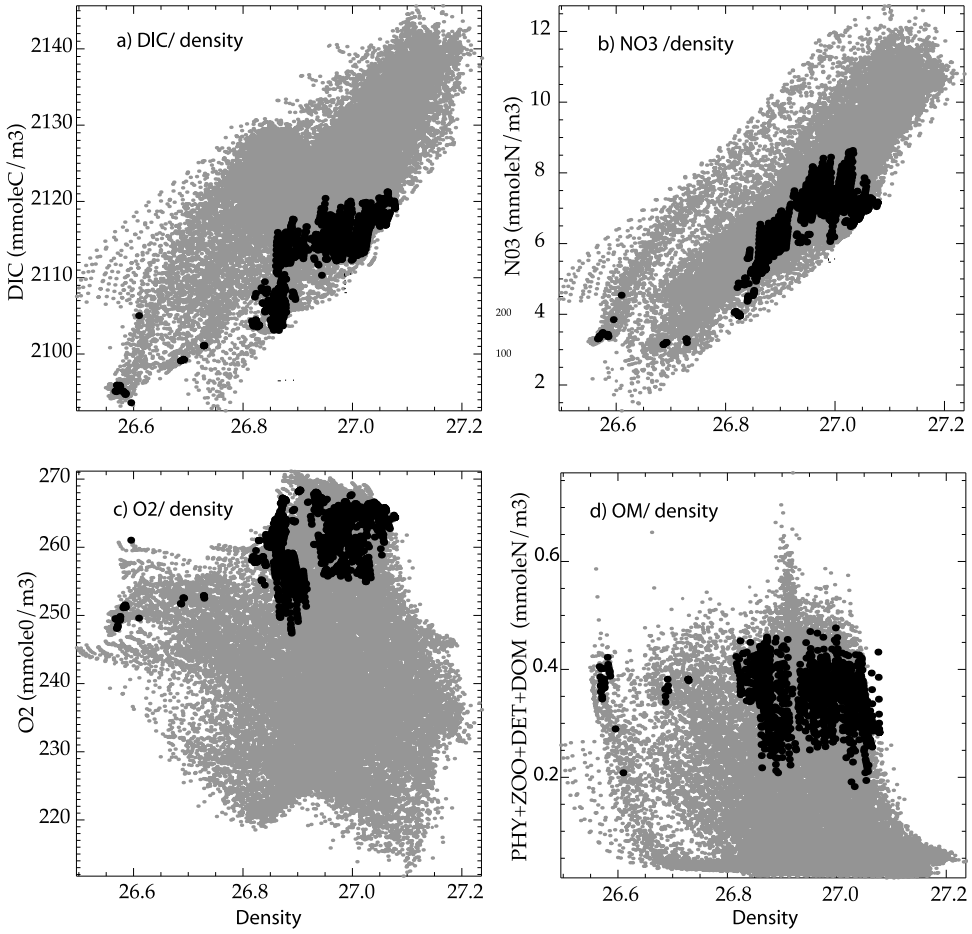

Figure 9. Scatterplot of density versus (a) DIC, (b) nitrate, (c) oxygen, and (d) organic matter (OM), within the depth range 100–250 m, after subduction on 24 May 2001 (i.e., at the time of Figure 8). The black dots mark NEAMW, i.e., where potential density is less than 8×10^{-11} m^{-1}.

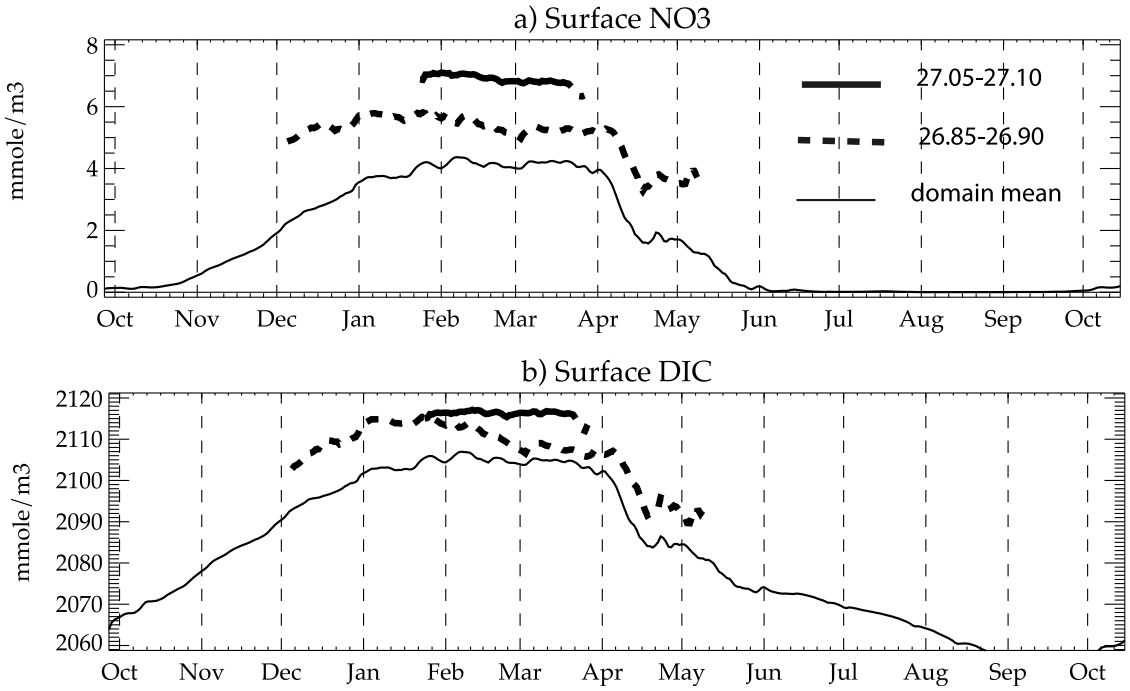

Figure 10. Time evolution of (a) nitrate and (b) DIC concentration at the surface, averaged over waters with surface density in the ranges 26.85–26.90 (dashed line) and 27.05–27.10 (solid line). For comparison, the thin line shows the average surface concentration over the whole POMME domain.

the bloom) and continue to subduct in April during the bloom (Figures 6b and 6c).The surface winter concentrations in this density range are comparatively lower (Figure 10) because it is found farther south where nutrients are less (Figure 3). Moreover, the surface concentrations tend to decrease before subduction is completed, but this nutrient consumption prior to subduction is moderate (Figure 10).

[37] The biogeochemical characteristics of NEAMW are thus essentially those of surface winter values of DIC, nitrates, and oxygen, because subduction occurs essentially in winter when primary production is still low and when nutrients are abundant. There is no significant production within subsurface waters that further affects these characteristics. They cover a wide range of concentrations, which correspond essentially to the range of prebloom surface concentrations in the density range of NEAMW. The rest of subduction, occurring later in the season, injects waters with lower nutrient content and with organic material, but in moderate proportion. Our model results, indicating a moderate consumption of nutrients prior to subduction, are consistent with data estimations of preformed nutrients during POMME [*Reverdin et al.*, 2009].

5. Discussion

5.1. Annual Budgets and Functioning of the Carbon Pump

[38] In this section, an integrated view of how carbon and nitrogen are exported out of the mixed layer is presented. This analysis is based on model-derived annual budgets and fluxes across the mixed-layer base (Figure 11). It enables us to quantify the physical and biological carbon pumps. The large-scale circulation, oriented from the northwest to the southeast (Figure 2), induces a net inflow of 77 m yr^{-1} at the northern and western boundaries. Approximately half (34 m yr^{-1}) of this flow is subducted out of the mixed layer within the POMME domain; the remaining (43 m yr^{-1}) fluxes out at the southern and eastern boundaries (Figure 11a).

[39] To a large extent, carbon fluxes are analogous to water fluxes (Figure 11b): there is an inflow of 160 mol C m^{-2} yr^{-1} at the northwest; 57% of this inflow (92 mol C m^{-2} yr^{-1}) outflows at the southeast, and 41% (66 mol C m^{-2} yr^{-1}) is subducted out of the mixed layer within the POMME domain. These large-scale transports concern essentially DIC, the dominant form of carbon in the model. In addition, there is a net uptake of carbon through gas exchange at the sea surface of 1 mol C m^{-2} yr^{-1} and a net export through sedimentation of organic particles of 2 mol C m^{-2} yr^{-1}.

[40] These figures are roughly consistent with complementary estimates made on the basis of POMME observations. Regarding carbon subduction, our result of 66 mol C m^{-2} yr^{-1} corresponds to a net export of carbon of 0.283 pg C yr^{-1} to the inner ocean over the POMME domain (0.276 pg C yr^{-1} for DIC alone). This result is close to the 0.25 pg C yr^{-1} estimate of *Gonzalez-Davila et al.* [2005] for DIC subduction. We note, however, that *Gonzalez-Davila et al.*'s [2005] value was obtained by multiplying the end-winter DIC concentration by the climatological, annual subduction rate estimated by *Valdivieso da Costa et al.* [2005]. The same empirical method applied to our model results provides a slightly different estimate of 0.302 pg C yr^{-1}, underlining the role of the temporal and spatial evolution of DIC in the subduction. Regarding the air-sea CO_2 flux, *Gonzalez-Davila et al.* [2005], by extrapolation of in situ measurements, estimated an annual flux of 1.1 mol C m^{-2} yr^{-1}, also in agreement with the climatological estimate of *Takahashi*

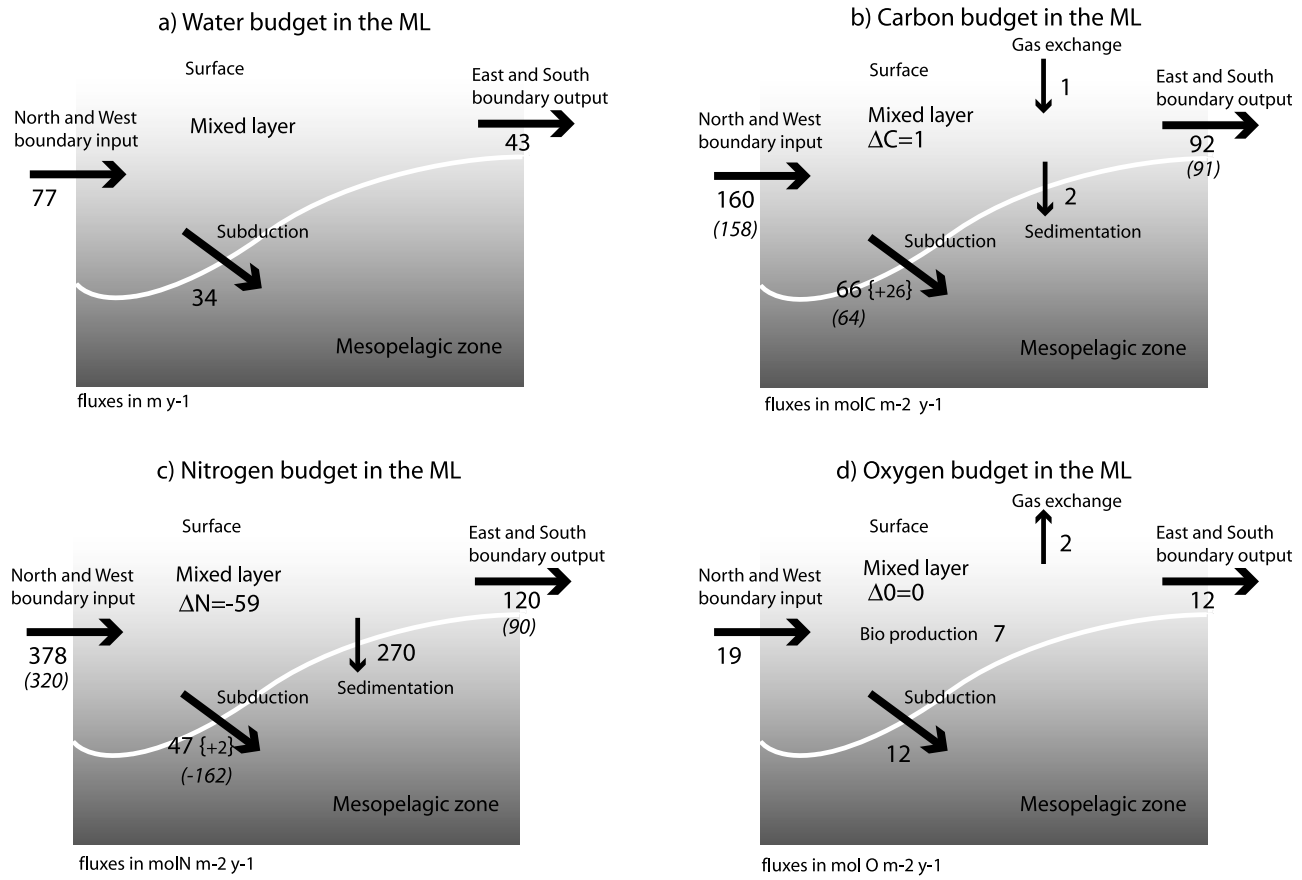

Figure 11. Budget and fluxes in the mixed layer (ML) during 1 year for (a) water, (b) carbon, (c) nitrogen, and (d) oxygen. The horizontal arrows show the advective fluxes across the open boundaries of the domain. The diagonal arrow is the total subduction across the mixed layer (white contour). Vertical arrows are the air-sea flux of carbon and oxygen due to gas exchange, and the sedimentation of detritus across the mixed layer. The Δ terms are the variations of the content over 1 year. For carbon and nitrogen, numbers represent the total fluxes, including organic and inorganic forms. Fluxes for DIC and dissolved inorganic nitrogen (DIN) alone are given in parentheses. For carbon and nitrogen, the extra subduction terms indicated between curly brackets correspond to the estimation of the subduction of the more refractory dissolved organic material compounds, which are not explicitly accounted for in the model.

et al. [2002] (1.0 mol C m^{-2} yr^{-1}) for this region. Our model results thus confirm the fact that the region acts as a sink of atmospheric carbon of approximately 1.0 mol C m^{-2} yr^{-1}.

[41] The model flux budget does not account for subduction of more refractory forms of organic material, since only semilabile DOM is accounted for in our model. Subduction of refractory and semirefractory DOC can be estimated from total organic carbon estimates made during POMME [*Sohrin and Sempéré*, 2005]. According to these measurements, there is a background refractory DOC concentration of ~500 mmolC m^{-3} throughout the water column, with an additional semirefractory pool of ~300 mmolC m^{-3} in the surface layer. Subduction of these two compounds can be roughly estimated based on model-derived DIC subduction. Subduction of DIC is due to the subduction of a volume of water (33.6 m yr^{-1}) whose average DIC concentration is 2100 mmolC m^{-3} (i.e., 71 mol C m^{-2} yr^{-1}), modulated by DIC gradients of order −200 mmolC m^{-3}. Given that the net subduction of DIC is 64 mol C m^{-2} yr^{-1}, the modulation by the gradients corresponds to a decrease of 71 − 64 = 7 mol C m^{-2} yr^{-1} (i.e., ~10%). Applied to refractory DOC, given a background value of 500 mmolC m^{-3} (i.e., ~25% of DIC) and a gradient of ~300 mmolC m^{-3} (i.e., ~150% of the DIC gradient), this gives an estimate for the subduction of the more refractory forms of DOC subduction of 64 × 0.25 + 7 × 1.5 = 26.5 mol C m^{-2} yr^{-1} (Figure 11b). If we consider a Redfield ratio of 12 for refractory DOM, this flux translates into ~2 mol N m^{-2} yr^{-1} (Figure 11c).

[42] The transfer of this air-sea flux of carbon to the ocean interior is generally explained in terms of the physical and biological carbon pumps. The biological pump is associated with the growth and subsequent sinking of phytoplankton. In this model, it corresponds to the sinking flux of detritus across the mixed layer. The physical pump is associated with the transport of carbon to the deeper ocean by the ocean circulation. In this situation, it corresponds to the amount of carbon being subducted, under organic or inorganic form. In terms of carbon export, our model emphasizes two important results. The first result is that the physical pump of labile organic carbon has the same magnitude as the biological pump (2 mol

Table A1. Biological Equations in the Euphotic Layer

Description	Equation
Nitrate source/sink	$S(NO_3) = -\mu_p L_I L_{NO_3} P + \mu_n NH_4$
Ammonium source/sink	$S(NO_4) = f_n \gamma \mu_p L_I (L_{NO_3} + L_{NH_4}) P - \mu p L_I L_{NH_4} P - \mu_n NH_4 + f_n(\mu_z Z + \mu_D D + \mu_{DOM} DOM)$
Phytoplankton source/sink	$S(P) = (1-\gamma)\mu_p L_I (L_{NO_3} + L_{NH_4}) P - G_p - m_p P$
Zooplankton source/sink	$S(Z) = a_z(G_p + G_d) - m_z Z^2 - \mu_z Z$
Detritus source/sink	$S(D) = (1-a_z)(G_p + G_d) + m_p P - G_d + f_z m_z Z^2 - \mu_d D - V_d \partial_z D$
DOM source/sink	$S(DOM) = (1-f_n)(\gamma \mu_p L_I (L_{NO_3} + L_{NH_4}) P + \mu_z Z + \mu_d D) - \mu_{DOM} DOM$
DIC source/sink	$S(DIC) = \alpha_d \mu_p Rd_{phy} D + \alpha_d \mu_z Rd_{phy} Z + \mu_{DOM} Rd_{DOM} DOM + ech_{gas} - \mu_p L_I (L_{NO_3} + L_{NH_4}) Rd_{phy} (1 + \rho_{CaCO_3}) P$
ALK source/sink	$S(ALK) = \mu_p L_I L_{NO_3} P - 2\rho_{CaCO_3} \mu_p L_I (L_{NO_3} + L_{NH_4}) Rd_{phy} P$
Oxygen source/sink	$S(OXY) = \mu_p L_I (L_{NO_3} Rd_{oxy} - (Rd_{oxy} - O/N_{nit}) S(NH_4) - Rd_{OXY} \mu_n NH_4$
Chlorophyll	$Chl = R_{chl:N} P$
Chlorophyll:nitrogen ratio	$R_{Chl:N} = \max(R^{min}_{Chl:N}, R^{max}_{Chl:N} - (R^{max}_{Chl:N} - R^{min}_{Chl:N}) \frac{\overline{PAR}}{PAR_{max}}$
Light limitation	$L_I = 1 - e^{\frac{PAR\, R_{Chl:N}}{K_{PAR} R^{ref}_{Chl:N}}}$
Nitrate limitation	$L_{NO_3} = \frac{NO_3}{NO_3 + K_{NO3}} e^{-\psi NH_4}$
Ammonium limitation	$L_{Nh_4} = \frac{NH_4}{NH_4 + K_{NH4}}$
Grazing of phytoplankton	$G_p = g_z \frac{pP}{K_z + pP + (1-p)D} Z$
Grazing of detritus	$G_p = g_z \frac{(1-p)D}{K_z + pP + (1-p)D} Z$
Preference for phytoplankton	$p = \frac{\tilde{p}P}{\tilde{p}P + (1-\tilde{p})D}$
Air-sea flux	$f_{gas} = k(Sc, u) sol(SST, SSS)[p^{atm}_{gas} - p^{ocean}_{gas}]$
Exchange coefficient	$k(Sc, u) = 0.31 u^2 (\frac{Sc}{660})^{-0,5}$
Schmidt number	$Sc = \frac{\nu}{D}$

Table A2. Biological Parameters

Parameter Name	Symbol	Value	Unit
Nitrate limitation half-saturation value	K_{NO_3}	0.7	mmol m^{-3}
Ammonium limitation half-saturation value	K_{NH_4}	0.001	mmol m^{-3}
Inhibition of nitrate uptake by ammonium	ψ	3	
Light limitation half-saturation value	K_{PAR}	33	W m^{-2}
Phytoplankton maximal growth rate	μ_p	1.21×10^{-5}	s^{-3}
Phytoplankton exudation rate	γ	0.05	
Phytoplankton mortality rate	m_p	5.80×10^{-7}	s^{-1}
Grazing half-saturation value	K_z	1	mmol m^{-3}
Zooplankton maximal grazing rate	g_z	9.26×10^{-6}	s^{-1}
Assimilated food fraction by zooplankton	a_z	0.7	
Preference for phytoplankton	$\tilde{p}$	0.5	
Zooplankton excretion rate	μ_z	5.80×10^{-7}	s^{-1}
Zooplankton mortality rate	m_z	2.31×10^{-6}	s^{-1} mmol^{-1} m^3
Fraction of slow sinking mortality	f_z	1	
Nitrification rate	μ_n	5.80×10^{-7}	s^{-1}
DOM breakdown rate	μ_{DOM}	3.86×10^{-7}	s^{-1}
Ammonium/DOM redistribution ratio	f_n	0.75	
Detritus sedimentation speed	V_d	3.47×10^{-5}	m s^{-1}
Detritus remineralization rate	μ_d	5.78×10^{-7}	s^{-1}
Minimum Chl:N ratio	$R^{min}_{Chl:N}$	1	mg Chl/mmolN
Maximum Chl:N ratio	$R^{max}_{Chl:N}$	2.62	mg Chl/mmolN
Reference Chl:N ratio	$R^{ref}_{Chl:N}$	1.31	mg Chl/mmolN
Max PAR for Chl:N ratio	PAR_{max}	5	W m^{-2}
C:N ratio for PHY, ZOO, DET	$Rd_{phy} = 6.625$		
C:N ratio for DOM	$Rd_{DOM} = 12$		
O:N ratio for nitrification	$Rd_{nit} = 2$		
O:N ratio for primary production	$Rd_{oxy} = 10.75$		
Atmospheric p_{CO_2}	$p^{atm}_{CO_2} = 375$		μatm
Atmospheric p_{CO_2}	$p^{atm}_{CO_2} = 209.46$		μatm

Table A3. Optical Model

Description	Equation
Wavelength decomposition	$PAR = PAR_r + PAR_b$; $PAR_r(0) = \frac{0.43}{2} Q_{sol}$; $PAR_b(0) = \frac{0.43}{2} Q_{sol}$
Light absorption in red	$PAR_r(z) = PAR_r(z - dz) e^{-k_r dz}$
Light absorption in blue	$PAR_b(z) = PAR_b(z - dz) e^{-k_b dz}$
Absorption coefficient in red	$k_r = k_{r0} + \chi_{rp} Pig^{e_r}$
Absorption coefficient in blue	$k_b = k_{r0} + \chi_{bp} Pig^{e_b}$
Absorbing pigments	$Pig = \frac{Chl}{r_{pig}}$

Table A4. Optical Parameters

Symbol	Value	Units
k_{r0}	0.225	m^{-1}
k_{b0}	0.0232	m^{-1}
χ_{rp}	0.037	m^{-1} (mg Chl m^{-3})$^{-e_r}$
χ_{bp}	0.074	m^{-1} (mg Chl m^{-3})$^{-e_b}$
e_r	0.629	
e_b	0.674	
r_{pig}	0.7	

C m^{-2} yr^{-1} each). This total export of labile organic carbon is equal to four times the air-sea exchange (1 mol C m^{-2} yr^{-1}).

[43] The second result is the importance of the physical pump of both organic and inorganic carbon. According to our estimates, the total amount of carbon exported below the mixed layer is shared among subduction of inorganic carbon (70%), subduction of organic carbon (28%), and detritus sedimentation (2%). The large contribution of subduction (the physical pump) is explained by the large background values of DIC and refractory DOC that pass through the winter MLD gradient. At the scale of the Atlantic basin, they should be compensated by an induction flux of DIC and DOC (the reverse of the subduction process) in areas of induction, such as along the western boundary current [*Williams et al.*, 2006]. At the scale of an ocean basin, our results thus emphasize that the net export of carbon represents a small fraction of the fluxes of carbon across the mixed layer through the processes of subduction and induction. At the scale of the POMME region, known as a sink for atmospheric CO_2, our results highlight the important role of subduction in exporting carbon, under both organic and inorganic forms.

[44] The nitrogen budget is fairly different from the carbon budget. Subduction of nitrogen represents only 15% of the total input at the northwest boundaries of the POMME domain. As mentioned before, an important difference with carbon is that, on average, nitrogen is subducted in its organic form, while there is a net obduction of inorganic nitrogen. In fact, there is also subduction of inorganic nitrogen, but this subduction is restricted to the density range of NEAMW (Figure 7). Moreover, the fact that a significant fraction of the nitrate obducted in this region is unutilized and simply resubducted reflects an interesting inefficiency in nutrient utilization and limitation on the effectiveness of biological carbon sequestration in the gyre.

[45] Regarding oxygen, there is a net subduction of 12 mol O m^{-2} yr^{-1} that leads to the ventilation of the thermocline. This net subduction represents 63% of the input flux at the northwest. This larger proportion, compared to water and DIC, is linked to the fact the oxygen is also produced in the mixed layer by biological activity (7 mol O m^{-2} yr^{-1}) and partly outgassed to the atmosphere (2 mol O m^{-2} yr^{-1}).

5.2. Transfer of Nutrients to the Subtropical Gyre

[46] Two different types of mode waters, formed in the North Atlantic, are found in the North Atlantic subtropical gyre: the NEAMW, which were the focus of the POMME program and are formed on the eastern side of the North Atlantic, and the subtropical mode waters (STMW), also know as 18°C water, formed on the western side, just south of the Gulf Stream extension [*Worthington*, 1959]. These two mode waters fuel the mesopelagic nutrient reservoir of the subtropical gyre. Their biogeochemical characteristics are thus of primary importance for the productivity of the gyre.

[47] Our results suggest that subduction of NEAMW efficiently contributes to the fueling of the nutrient reservoir of the subtropical gyre, provided that they are obducted in a different region than the region where they are subducted. This result ensues from the fact that they are mostly subducted in winter, prebloom conditions. They are thus rich in nutrients when they subduct. This finding is supported by the analysis of in situ POMME data focused on NEAMW by *Reverdin et al.* [2009]. Regarding STMW, a contrasting result was reported. *Palter et al.* [2005] indeed observed that STMW are significantly depleted in nutrients in comparison with nearby water masses. The modeling study of *Kremeur et al.* [2009] suggests that this is because STMW are formed by subduction toward the end of the spring bloom. Thus, in the case of STMW, subducting waters have been more efficiently depleted in nutrients before they leave the surface.

[48] The difference in nutrient content between NEAMW and STMW can in fact be rationalized in terms of the different production regimes of the two regions where these mode waters are formed [*Lévy et al.*, 2005a]. The region of NEAMW formation is dominated by a subpolar production regime: in such a regime, the bloom is light-limited and starts when the mixed layer retreats. The region of STMW formation is dominated by a subtropical production regime: in this case, production is nutrient-limited and the bloom starts earlier, when the mixed layer deepens. The nutrient reservoir of the North Atlantic subtropical gyre is thus fueled on the eastern side by nutrient-rich NEAMW and on the western side by nutrient-poor STMW. This east-west contrast in subsurface nutrient fueling may explain the east-west contrast in productivity observed in the North Atlantic subtropical

Table A5. Remineralization Equations Below the Euphotic Layer

Description	Equation
Nitrate source/sink	$S(NO_3) = \tau_r(NH_4 + P + Z + D + DOM) + \partial_z f$
Ammonium source/sink	$S(NH_4) = -\tau_r NH_4$
Phytoplankton source/sink	$S(P) = -\tau_r P$
Zooplankton source/sink	$S(Z) = -\tau_r Z$
Detritus source/sink	$S(D) = -\tau_r D - V_d \partial_z D$
DOM source/sink	$S(DOM) = -\tau_r DOM$
Remineralization flux	$f(z) = f(z_{bio})(\frac{z}{z_{bio}})^{-r}$
Instantaneous export	$f(z_{bio}) = \int_0^{z_{bio}} (1 - f_z) m_z Z^2 \, dz$
No floor deposition	$f(z_{bottom}) = 0$

Table A6. Remineralization Parameters

Parameter Name	Symbol	Value	Units
Depth of euphotic layer	z_{bio}	150	m
Bottom topography	z_{bottom}	variable	m
Remineralization rate at depth	τ_r	5.80×10^{-7}	s^{-1}
Exponential decay	r	0.858	

gyre, with higher productivities in the east than in the west [*Lévy*, 2005].

6. Conclusion

[49] With several oceanic cruises covering the seasonal cycle, the POMME program was aimed to investigate the process of NEAMW formation and their biogeochemical characterization. The large amount of data collected during POMME enabled the construction of a biophysical model for the area, constrained by the observations. This model was used to provide synthetic budgets of carbon, nitrogen, and oxygen over the POMME region, with a particular focus on subduction fluxes.

[50] Our analysis highlights the predominant role of subduction in exporting carbon below the mixed layer. Carbon subduction accounts for 98% of total carbon export; the other 2% is due to the sedimentation of organic particles. This large subduction flux has to be compensated by an obduction flux of similar magnitude elsewhere in the North Atlantic basin. Moreover, the export of labile organic material is also largely affected by subduction: while 50% of labile organic carbon export is achieved through the classical sedimentation of detritus, we found that the other 50% is due to the subduction of labile organic material, mainly at the beginning of the bloom.

[51] Finally, we found that NEAMW constitute a significant nutrient reservoir for the subtropical gyre. This is because NEAMW are essentially subducted in winter (i.e., in prebloom conditions). They are thus rich in nutrients when they subduct. We note that this reflects a certain degree of inefficiency in nutrient utilization in the region of NEAMW formation. This is contrary to STMW, which are nutrient-poor when they are formed. This difference between NEAMW and STMW might partly explain the larger productivities observed in the eastern part of the North Atlantic subtropical gyre compared to the western part.

[52] The analysis presented in this paper mainly focused on the integrated subduction fluxes after 1 year. The two main terms contributing to subduction were lateral induction and vertical advection. Further analysis of our model results revealed that these terms are highly variable at the submesoscale [*Karleskind*, 2009]. A more detailed analysis of this variability and of its implications is the focus of a subsequent paper [*Karleskind et al.*, 2011].

Appendix A: Biogeochemical Model

[53] We use the same biological model as *Resplandy et al.* [2009]. The model equations and parameters are recalled in Tables A1, A2, A3, A4, A5, and A6.

[54] **Acknowledgments.** M.L. is the corresponding author. This work is part of P.K.'s Ph.D. thesis, which was supported by DGA. We thank all participants in the POMME program for making their data available to us. POMME was supported by CNRS-INSU (POMME and TWISTED programs). Extremely valuable comments from two anonymous reviewers helped in reconsidering some of our preliminary interpretations.

References

Caniaux, G., A. Brut, D. Bourras, H. Giordani, A. Paci, L. Prieur, and G. Reverdin (2005), A 1 year sea surface heat budget in the northeastern Atlantic basin during the POMME experiment: 1. Flux estimates, *J. Geophys. Res.*, *110*, C07S02, doi:10.1029/2004JC002596.

Cushman-Roisin, B. (1987), Subduction, in *Dynamics of the Oceanic Surface Mixed Layer*, edited by P. Müller and D. Henderson, pp. 181–196, Hawaii Inst. of Geophys., Honolulu.

de Boyer Montegut, C., G. Madec, A. S. Fischer, A. Lazar, and D. Iudicone (2004), Mixed layer depth over the global ocean: An examination of profile data and a profile-based climatology, *J. Geophys. Res.*, *109*, C12003, doi:10.1029/2004JC002378.

Gaillard, F., H. Mercier, and C. Kermabon (2005), A synthesis of the POMME physical data set: One year monitoring of the upper layer, *J. Geophys. Res.*, *110*, C07S07, doi:10.1029/2004JC002764.

Gaspar, P., Y. Gregoris, and J.-M. Lefevre (1990), A simple eddy kinetic energy model for simulations of the oceanic vertical mixing: Tests at station Papa and Long-Term Upper Ocean Study site, *J. Geophys. Res.*, *95*(C9), 16,179–16,193.

Gavart, M., P. de Mey, and G. Caniaux (1999), Assimilation of satellite altimeter data in a primitive-equation model of the Azores-Madeira region, *Dyn. Atmos. Oceans*, *29*, 217–254.

Giordani, H., G. Caniaux, L. Prieur, A. Paci, and S. Giraud (2005), A 1 year mesoscale simulation of the northeast Atlantic: Mixed layer heat and mass budgets during the POMME experiment, *J. Geophys. Res.*, *110*, C07S08, doi:10.1029/2004JC002765.

Gonzalez-Davila, M., J. M. Santana-Casiano, L. Merlivat, L. Barbero-Munoz, and E. V. Dafner (2005), Fluxes of CO_2 between the atmosphere and the ocean during the POMME project in the northeast Atlantic Ocean during 2001, *J. Geophys. Res.*, *110*, C07S11, doi:10.1029/2004JC002763.

Goutx, M., C. Guigue, N. Leblond, A. Desnues, A. Dufour, D. Aritio, and C. Guieu (2005), Particle flux in the northeast Atlantic Ocean during the POMME experiment (2001): Results from mass, carbon, nitrogen, and lipid biomarkers from the drifting sediment traps, *J. Geophys. Res.*, *110*, C07S20, doi:10.1029/2004JC002749.

Guieu, C., M. Roy-Barman, N. Leblond, C. Jeandel, M. S. B. L. Cann, A. Dufour, and C. Bournot (2005), Vertical particle flux in the northeast Atlantic Ocean (POMME experiment), *J. Geophys. Res.*, *110*, C07S18, doi:10.1029/2004JC002672.

Karleskind, P. (2009), Caracterisation des eaux modales de l atlantique nord-est: ventilation de la thermocline et flux biogeochimiques, Ph.D. thesis, Univ. Bretagne Occidentale, Brest, France.

Karleskind, P., M. Lévy, and L. Memery (2011), Modifications of mode water properties by sub-mesoscales in a bio-physical model of the northeast Atlantic, *Ocean Modell.*, doi:10.1016/j.ocemod.2010.12.003, in press.

Kremeur, A.-S., M. Lévy, O. Aumont, and G. Reverdin (2009), Impact of the subtropical mode water biogeochemical properties on primary production in the North Atlantic: New insights from an idealized model study, *J. Geophys. Res.*, *114*, C07019, doi:10.1029/2008JC005161.

Lévy, M. (2005), Nutrients in remote mode, *Nature*, *437*, 628–629.

Lévy, M., Y. Lehahn, J.-M. Andre, L. Memery, H. Loisel, and E. Heifetz (2005a), Production regimes in the northeast Atlantic: A study based on Sea-viewing Wide Field-of-view Sensor (SeaWiFS) chlorophyll and ocean general circulation model mixed layer depth, *J. Geophys. Res.*, *110*, C07S10, doi:10.1029/2004JC002771.

Lévy, M., M. Gavart, L. Memery, G. Caniaux, and A. Paci (2005b), A four-dimensional mesoscale map of the spring bloom in the northeast Atlantic (POMME experiment): Results of a prognostic model, *J. Geophys. Res.*, *110*, C07S21, doi:10.1029/2004JC002588.

Marshall, J. C., A. J. G. Nurser, and R. G. Williams (1993), Inferring the subduction rate and the period in the North Atlantic, *J. Phys. Oceanogr.*, *23*, 1315–1329.

Memery, L., G. Reverdin, J. Paillet, and A. Oschlies (2005), Introduction to the POMME special section: Thermocline ventilation and biogeochemical tracer distribution in the northeast Atlantic Ocean and impact of mesoscale dynamics, *J. Geophys. Res.*, *110*, C07S01, doi:10.1029/2005JC002976.

Paci, A., G. Caniaux, M. Gavart, H. Giordani, M. Lévy, L. Prieur, and G. Reverdin (2005), A high-resolution simulation of the ocean during the POMME experiment: Simulation results and comparison with observations, *J. Geophys. Res.*, *110*, C07S09, doi:10.1029/2004JC002712.

Paci, A., G. Caniaux, H. Giordani, M. Lévy, L. Prieur, and G. Reverdin (2007), A high-resolution simulation of the ocean during the POMME

experiment: Mesoscale variability and near surface processes, *J. Geophys. Res.*, *112*, C04007, doi:10.1029/2005JC003389.
Paillet, J., and M. Arhan (1996), Oceanic ventilation in the eastern North Atlantic, *J. Phys. Oceanogr.*, *26*, 2036–2052.
Palter, J. B., M. S. Lozier, and R. T. Barber (2005), The effect of advection on the nutrient reservoir in the North Atlantic subtropical gyre, *Nature*, *437*, 687–692.
Qiu, B., and R. Huang (1995), Ventilation of the North Atlantic and North Pacific: Subduction versus obduction, *J. Phys. Oceanogr.*, *25*, 2374–2390.
Resplandy, L., M. Lévy, F. d'Ovidio, and L. Merlivat (2009), Impact of submesoscale variability in estimating the air-sea CO_2 exchange: Results from a model study of the POMME experiment, *Global Biogeochem. Cycles*, *23*, GB1017, doi:10.1029/2008GB003239.
Reverdin, G., M. Assenbaum, and L. Prieur (2005), Eastern North Atlantic mode waters during POMME (September 2000–2001), *J. Geophys. Res.*, *110*, C07S04, doi:10.1029/2004JC002613.
Reverdin, G., M. Lévy, P. Raimbault, and D. Lefevre (2009), Nutrients in mode waters of the northeast Atlantic, *J. Geophys. Res.*, *114*, C10004, doi:10.1029/2009JC005546.
Rios, A. F., T. R. Anderson, and F. F. Perez (1995), The carbonic system distribution and fluxes in the NE Atlantic during spring 1991, *Prog. Oceanogr*, *35*, 295–314.
Sarmiento, J. L., et al. (2004), Response of ocean ecosystems to climate warming, *Global Biogeochem. Cycles*, *18*, GB3003, doi:10.1029/2003GB002134.
Sohrin, R., and R. Sempéré (2005), Seasonal variation in total organic carbon in the northeast Atlantic in 2000–2001, *J. Geophys. Res.*, *110*, C10S90, doi:10.1029/2004JC002731.
Takahashi, T., T. T. Takahashi, and S. C. Sutherland (1995), An assessment of the role of the North Atlantic as a CO_2 sink, *Philos. Trans. R. Soc. London, Ser. B*, *348*, 143–152.
Takahashi, T., et al. (2002), Global sea-air CO_2 flux based on climatological surface ocean p_{CO_2}, and seasonal biological and temperature effects, *Deep Sea Res. Part II*, *49*, 1601–1622.
Valdivieso da Costa, M., H. Mercier, and A.-M. Treguier (2005), Effects of the mixed layer time variability on kinematic subduction rate diagnostics, *J. Phys. Oceanogr.*, *35*, 427–443.
Williams, R., V. Roussenov, and M. Follows (2006), Nutrient streams and their induction into the mixed layer, *Global Biogeochem. Cycles*, *20*, GB1016, doi:10.1029/2005GB002586.
Worthington, L. (1959), The 18° water in the Sargasso Sea, *Deep Sea Res.*, *5*, 297–305.

P. Karleskind and L. Memery, LEMAR, CNRS/IRD/UBO, F-29280 Brest, France.
M. Lévy, LOCEAN/IPSL, CNRS/UPMC/IRD/MNHN, 4 Pl. Jussieu, F-75252 Paris CEDEX 05, France. (marina@locean-ipsl.upmc.fr)